



www.adeepakpublishing.com

Alvarez et al. (2023): JoSS, Vol. 12, No. 2, pp. 1231–1247  
(Peer-reviewed article available at [www.jossonline.com](http://www.jossonline.com))



www.JoSSonline.com

# Design and On-Orbit Performance of the Attitude Determination and Passive Control System for the Quetzal-1 CubeSat

Dan Alvarez, Aldo Aguilar-Nadalini, José Bagur,  
Víctor Ayerdi, and Luis Zea

*Universidad del Valle de Guatemala  
Guatemala City, Guatemala*

---

## Abstract

Quetzal-1, a 1U CubeSat developed by Universidad del Valle de Guatemala, operated on orbit from April to November of 2020. It included an in-house developed passive attitude determination and control system (ADCS) based on a previous mission from a different team, the Colorado Student Space Weather Experiment (CSSWE). Quetzal-1's ADCS used a  $0.74 \text{ A} \cdot \text{m}^2$  magnet to align the satellite to Earth's magnetic field. Due to volumetric constraints, Quetzal-1 only incorporated two hysteresis rods in contrast to CSSWE, a 3U CubeSat that carried six of them. The rods were located on mutually orthogonal axes to stabilize its rotation. Earth's magnetic field inclination over Guatemala, the mission's geographical zone of interest, informed the location of the ADCS components and the camera with respect to the satellite's structure to maximize the probability of target image acquisition. A Singular Value Decomposition (SVD) method was implemented for attitude determination together with a three-axis magnetometer and two photodiodes on each of the satellite's six sides. Within a week of deployment from the International Space Station (ISS), Quetzal-1's ADCS was capable of stabilizing rotational rates from  $\pm 25^\circ/\text{s}$  to  $\pm 3.5^\circ/\text{s}$  per axis. Additionally, it correctly aligned the satellite to the magnetic field vector to within  $14.28^\circ$ . The ADCS' gyroscope operated nominally, while the magnetometer occasionally transmitted all-zero data at temperatures below  $10^\circ\text{C}$ . Most importantly, the ADCS enabled the payload to acquire images. The results and performance of Quetzal-1's ADCS, from per-component and systemic perspectives, are described in this manuscript, including the impact of flights over the South Atlantic Anomaly (SAA) on the magnet's torque and oscillation amplitudes. Detailed description of the design approach, component selection criteria, results, and recommendations based on lessons learned may be valuable to other teams developing their own CubeSat passive ADCS.

---

## 1. Introduction

Quetzal-1 (ket-sahl-oo-noh) was a 1U CubeSat developed by Universidad del Valle de Guatemala

(UVG) and supported, in terms of its launch to and deployment from the International Space Station (ISS), by the United Nations Office for Outer Space Affairs (UNOOSA) and the Japan Aerospace Exploration

Corresponding Author: Luis Zea – [lpzea@uvg.edu.gt](mailto:lpzea@uvg.edu.gt) / Víctor Ayerdi – [vhayerdi@uvg.edu.gt](mailto:vhayerdi@uvg.edu.gt)

Publication History: Submitted – 10/30/21; Revision Accepted – 12/0/22; Published – 05/31/23

Agency (JAXA) under their joint KiboCUBE Programme (Taniguchi et al., 2020). Quetzal-1's mission was selected to maximize benefits while considering programmatic risk and technical feasibility (Zea et al., 2016). The satellite's technical mission was to test a multispectral imaging system capable of acquiring images at different wavelengths by rotating a carousel carrying four light filters in front of a monochromatic camera. The systems engineering approaches implemented on this project are described by Martínez et al. (2018), the multispectral payload by Zea et al. (2023), the Electrical Power System (EPS) by Aguilar-Nadalini et al. (2023), the structure's Finite Element Analysis by Birnie et al. (2023), and the Command & Data Handling System (CDHS) by Chung et al. (2023).

The design of the Attitude Determination and Control System (ADCS) followed a passive approach due to resource limitations, financial and otherwise. While active systems use an array of sensors and actuators in a closed control loop to compute and manage the satellite's attitude, passive systems rely on the satellite's innate characteristics, such as geometry and mass properties, to provide stabilization. Passive Magnetic Attitude Control (PMAC) systems, as coined by Gerhardt (2014), are particularly applicable to CubeSats. PMAC systems have been in place since the very early history of space exploration. Transit 1B became the very first satellite to achieve orbit with such a system in place. In this study, the system used by Transit 1B implemented the very same building blocks that current passive magnetic systems use today: a permanent magnet to align the satellite with Earth's magnetic field (essentially converting the satellite into a large compass) and high magnetic susceptibility ferromagnetic material placed orthogonal to the magnet's orientation to dampen the system (and thus remove energy over time) (Danchik, 1998). The main advantages of a PMAC system include the simplicity of installation, low mass and zero power use (Gerhardt, 2014). Given these advantages, a PMAC system was also implemented on Quetzal-1, following the design guidelines put forward by Gerhardt (2014) as part of his contributions to the ADCS on board the Colorado Student Space Weather Experiment (CSSWE) 3U CubeSat. Further reasoning and analysis for this implementation of a PMAC on Quetzal-1 was provided in Alvarez

(2019) as part of the undergraduate thesis upon which this manuscript is based.

The design and development of this subsystem is covered in Sections 2 and 3. Section 4 provides details regarding the on-orbit performance of the ADCS, as well as the effects of the South Atlantic Anomaly (SAA) on the system. Finally, conclusions and recommendations are provided to other teams who may be developing their own PMAC systems.

## **2. Attitude Control Design**

### **2.1. Generalities of a PMAC System**

A PMAC system relies on a permanent magnet and hysteresis material to align the satellite with Earth's magnetic field and stabilize its rotation, respectively. The permanent magnet tracks the magnetic field in a similar fashion to how a 3D pendulum oscillates around the gravity vector. This magnet provides the main control torques on the satellite, and its size and material are selected depending on the required strength (measured as the magnetic moment of the magnet). The required strength depends on the magnitude of the external disturbance torques that the satellite will experience while in orbit, as well as the needed degree of alignment between the satellite and Earth's magnetic field. At the same time, the hysteresis material provides damping to the system. The changing polarities of Earth's magnetic field throughout the orbit cause a delayed response in the hysteresis material's magnetization (obeying its hysteresis curve). The magnetic domains within the material shift along the orbit, which effectively converts some of the satellite's rotational energy into heat (Gerhardt, 2014).

#### **2.1.1. Magnet Sizing**

The first step taken for the design of Quetzal-1's Attitude Control System was to determine the required magnet's characteristics based on parameters such as the CubeSat's mass and the expected magnetic fields and external torques at a 400-km high LEO orbit. Two key variables that needed to be considered when sizing the magnet were its torque and its magnetic moment.

A permanent magnet's torque can be calculated with the following equation:

$$\vec{L}_B = \vec{m}_{magnet} \times \vec{B}, \quad (1)$$

where  $\vec{m}_{magnet}$  represents the magnetic moment of the permanent magnet and  $\vec{B}$  represents the magnetic field surrounding the magnet. As shown in Eqn.1, a larger magnet would have a larger torque when exposed to the same  $\vec{B}$ . The larger the torque, the easier it would be able to overcome external disturbances. However, an oversized magnet could also introduce undesirable high potential energy at the time of deployment, as well as saturate or decrease the useful range of any on-board magnetometers (Gerhardt, 2014). Therefore, it was necessary to estimate the expected external disturbances on orbit in order to select a magnet that was neither under- nor over-sized.

An equation to estimate the minimum magnetic moment  $\vec{m}_{min}$  required to overcome the expected external torques is presented in (Gerhardt, 2014), which is a modification of the equation presented by (Santoni and Zelli, 2009). It states:

$$\|\vec{m}_{magnet}\| \geq \|\vec{m}_{min}\| = 15 \left( \frac{\|\vec{L}_{sum}\|}{\|\vec{B}_{min}\| \cdot \sin \beta_{max}} \right), \quad (2)$$

where  $\|\vec{L}_{sum}\|$  is the sum of magnitudes of all external torques (not accounting for any magnetic residual torques, i.e. the magnetic moment of the satellite itself),  $\|\vec{B}_{min}\|$  is the minimum experienced magnetic field for the satellite's orbit and  $\beta_{max}$  is the desired angle of maximum oscillation of the satellite to Earth's magnetic field.

As evidenced in Eqn. 2, the estimation of all external torques is fundamental in determining the magnet's minimum required magnetic moment. The CubeSat Control Toolbox (Princeton Satellite Systems, 2010) was used to estimate these torques for the ISS orbit (from where Quetzal-1 would be deployed) via simulations of the on-orbit environment. Torques were simulated for an orientation perfectly aligned with the magnetic field, starting on January 1, 2019 at 00:00:00 UTC and ending on January 1, 2020 at 00:00:00 UTC, using the tilted dipole as the magnetic field model and selecting a 1U CubeSat with mass 1.04 kg and solar

panels on all six sides (see assumed optical parameters and other physical parameters in Table 2). These dates were used as a standardized timeframe because the launch date was unknown at the time of development of this subsystem. The maximum estimated torques are shown in Table 1.

Table 1. Maximum Estimated External Torques from Jan. 1, 2019 at 00:00:00 UTC to Jan. 1, 2020 at 00:00:00 UTC on ISS Path

Torque Type	Maximum Value (nN · m)
Aerodynamic	17.2
Solar Pressure Gravity	1.2
Gradient	0.5
Total	18.9

Table 2. Satellite Physical Parameters. Function *diag()* produces a diagonal matrix with the diagonal set to its arguments.

Parameter	Value
Center of Mass	[0.067, -1.577, 2.509] mm
Inertia	diag (1816, 1882, 1621) kg · mm <sup>2</sup>
Drag Coefficient	2.40
Solar panel optical coefficients:	
Transmissivity	0.00
Absorptivity	0.75
Reflectivity (specular)	0.17
Reflectivity (diffuse)	0.08

Two more parameters were needed to calculate the minimum necessary magnetic moment:  $\beta_{max}$  and  $\|\vec{B}_{min}\|$ . For the first, an arbitrary value of 5° was assigned, while for the latter – and to be conservative – the United States' National Oceanic and Atmospheric Administration (NOAA) magnetic field calculator (National Geophysical Data Center, n.d.) was used to determine the field strength where it may be expected to be at its weakest. Such a location was determined at an elevation of 400 km (over mean sea level) at an arbitrary date of January 1, 2020: -23° latitude and 58° longitude (above the South Atlantic Anomaly, or SAA) with a value of 19,133 nT. Finally, the minimum necessary magnetic moment for the magnet was calculated using Eqn. 2, resulting in  $\|\vec{m}_{min}\| = 0.1700 \text{ A} \cdot \text{m}^2$ . This value drove a requirement for the flight magnet selection; thus, a cylindrical magnet (K&J Magnet-

ics, Cat. No D84), with grade N42, 12.7 mm in diameter and 6.35 mm in height, was selected for Quetzal-1. This magnet was selected due to its flight heritage from the CCSWE mission and due to its dimensions, which were adequate for a 1U CubeSat. As part of Quetzal-1's requirement verification process, the magnetic moment of the magnet was measured experimentally following the procedure detailed by Gerhardt (2014), and was found to be  $\|\vec{m}_{magnet}\| = 0.7363 \text{ A m}^2 \geq \|\vec{m}_{min}\|$ , which is approximately four times larger than the required minimum magnetic moment. Due to time constraints, the magnet was ultimately deemed acceptable, but possible disadvantages of such an oversized magnet are discussed in Section 4.2.

### 2.1.2. PMAC System Errors

A PMAC system will exhibit two types of errors. The first is a steady-state error, in which the magnetic moment of the hysteresis material (and all other magnetic material on-board) adds in a vectorial fashion with the permanent magnet's magnetic moment. Thus, the satellite will no longer align perfectly with the magnetic moment of the magnet ( $\vec{m}_{magnet}$ ). Rather, it will align with the resulting magnetic moment ( $\vec{m}_{tot}$ ), which causes the satellite to offset from the magnetic field vector by an angle  $\gamma$  (as shown in Figure 1) (Gerhardt, 2014). Given that the PMAC system may only fully constrain two axes of rotation, a final roll rate is expected to appear along ( $\vec{m}_{tot}$ ).

The second is an oscillatory error caused by changes in magnetic field direction along the orbit. As the field changes, the magnet attempts to track it, but overshoots occur. The oscillatory error may be reduced by increasing the amount of hysteresis material (Santoni and Zelli, 2009), but such an increase leads to an increase in steady-state error. Hence, the final design of a PMAC system must adequately balance these two errors (Gerhardt, 2014).

### 2.1.3. Determining Magnet and Hysteresis Rod Location

As per standard PMAC system design requirements, Quetzal-1 used two HyMu-80, 95 mm in height and 1 mm in diameter, cylindrical hysteresis rods,

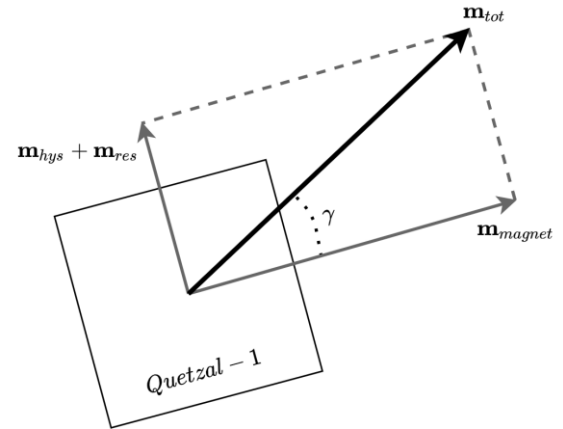


Figure 1. Total magnetic moment of a Passive Magnetic Attitude Control System ( $\vec{m}_{hys}$  is the magnetic moment of the hysteresis material,  $\vec{m}_{res}$  is the residual magnetic moment of the satellite itself, and  $\gamma$  is the offset of the total magnetic moment of the system,  $\vec{m}_{tot}$ , with respect to  $\vec{m}_{magnet}$ ).

which were selected according to their flight heritage in CSSWE and availability, and were placed in mutually orthogonal axes. The placement of these rods also needed to be orthogonal to the magnet's magnetic moment vector. Selecting the specific axes in which both the magnet and the rods were going to be placed was the next step of PMAC system design. Quetzal-1 contained an on-board camera, which had to be correctly aligned with Earth at the desired locations in order to take relevant imagery. In this case, the desired target was Guatemala, located between latitudes  $[13.75^\circ, 17.81^\circ]$  and longitudes  $[-92.21^\circ, -88.24^\circ]$ . According to Figure 2, the magnetic field inclination (the angle between local nadir and the magnetic field vector) was going to be roughly  $45^\circ$  over Guatemala.

The placement of the magnet drove the placement of the rods. Therefore, deciding whether the magnet was placed either parallel or perpendicular to the camera's boresight was of the utmost importance (see Figure 3). Considering the  $45^\circ$  magnetic field inclination over Guatemala, a parallel configuration had the immediate advantage of being more predictable. In that configuration, the camera would always face approximately towards the magnetic field vector, assuming that the PMAC system would detumble the satellite correctly. A perpendicular configuration, however, would be affected not only by correct detumbling, but

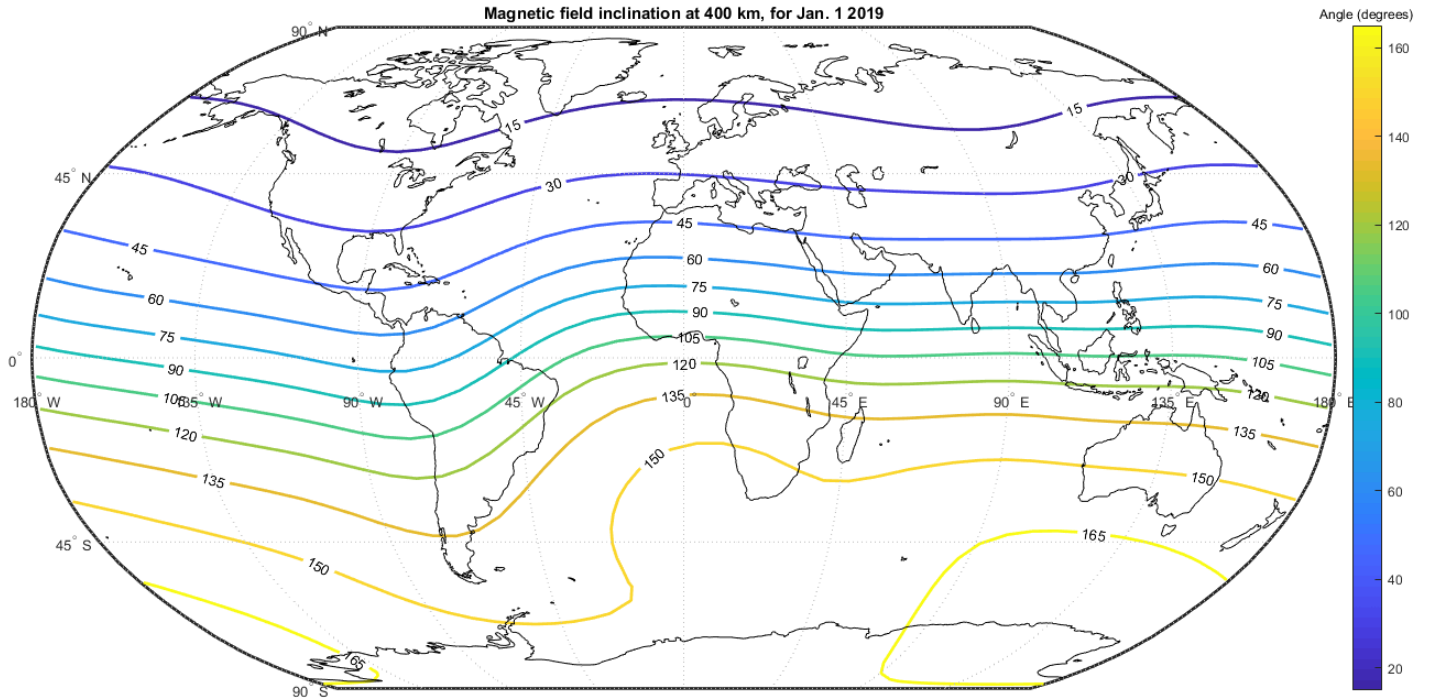


Figure 2. Magnetic field inclination at an altitude of 400 km. Note inclination over Guatemala is approximately 45°. Data calculated for January 1, 2019 with the `igrfmagm` implementation of IGRF-12 in MATLAB.

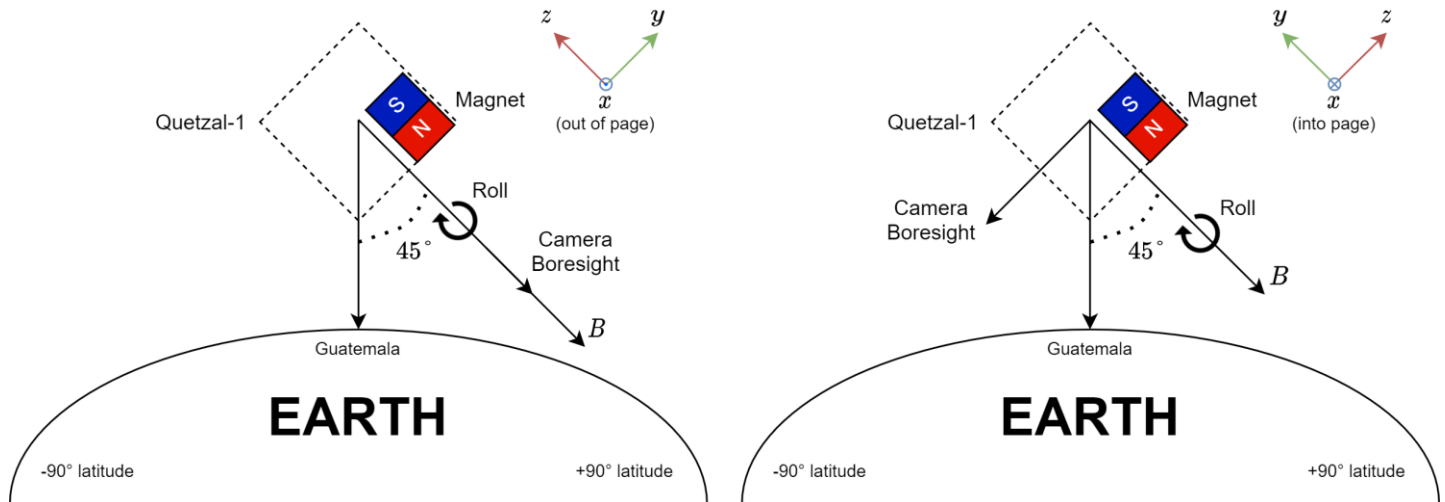


Figure 3. Parallel (left) and perpendicular (right) configurations of camera's boresight and permanent magnet assuming the ideal situation where  $\vec{B}$  is collinear with the satellite's roll axis and the magnet's magnetic moment vector,  $\vec{m}_{magnet}$ . Ultimately, a parallel configuration was selected. The satellite is moving in a prograde orbit (west to east) with the same inclination of the ISS orbit (velocity vector points out of the page).

also by the final roll rate of the system. Given the additional degree of uncertainty in the latter configuration, a parallel placement was chosen.

#### 2.1.4. PMAC System Physical Component Placement

The final positions for the ADCS components are shown in Figure 4. Note that the camera boresight was placed facing the  $-Z$  direction. Therefore, the hysteresis rods were placed collinear to the  $X$  and  $Y$  axes, while the permanent magnet's North pole faced the  $-Z$  direction, so the camera faced nadir when orbiting over the northern hemisphere. As to the physical

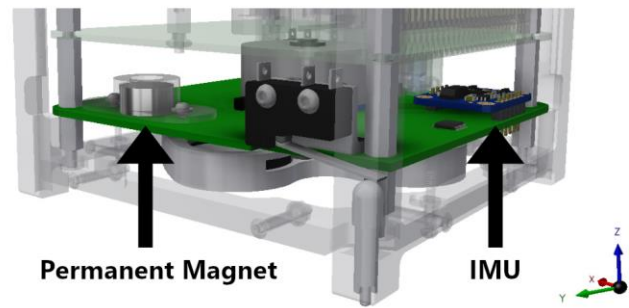
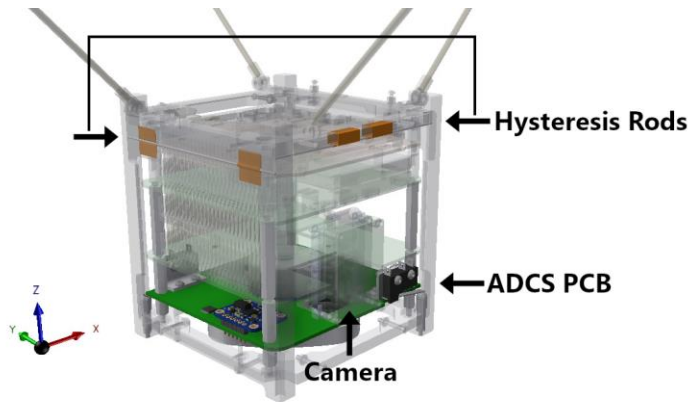


Figure 4: Location of the ADCS PCB containing the magnet, and the hysteresis rods inside the 1U CubeSat. Permanent magnet located on the (+X, +Y) corner of the PCB, IMU located on the (-X, -Y) corner, and Camera at the center of the satellite's -Y face, with its boresight pointing towards -Z.

placement of components in the ADCS printed circuit board (PCB), the permanent magnet was located on the same PCB as the magnetometer, due to space constraints within the satellite. However, distance between these was maximized to reduce hard-iron errors on the magnetometer, as the permanent magnet was placed in the (+X, +Y) corner of the PCB, while the Inertial Measurement Unit (IMU) was located diagonally opposite, on the (-X, -Y) corner. Note as well that the vertical distance between the ADCS PCB and the hysteresis rods was the maximum possible for the satellite design at 64.9 mm, aiming to minimize soft-iron errors on the IMU. Both hard-iron and soft-iron errors are defined in subsection 3.4.

### 3. Attitude Determination Design

#### 3.1. Attitude Determination Requirements

An Attitude Determination System requires a set of on-board sensors to attain attitude. A wide array of sensors can be implemented on a satellite, depending on power, volume and resolution constraints and requirements. Due to the passive nature of Quetzal-1's ADCS, real time attitude knowledge was not required, and power priority was relatively low, since other subsystems had higher criticality to operations and required more power. Hence, it was deemed that a three-axis magnetometer and a set of photodiodes on each of the CubeSat's six sides—to obtain the magnetic field

vector and the solar vector in the body frame, respectively—would be enough to compute the satellite's attitude through a deterministic approach such as the one detailed in the next subsection. This would also be enough to evaluate the performance of the PMAC throughout the mission, especially during picture-capture operations.

#### 3.2. Attitude Determination Approach

The typical approach for CubeSat missions on the matter of attitude determination involves the use of a Kalman Filter: a powerful, yet complex state estimation tool that enables a satellite to fuse sensor data to provide a more accurate picture of the satellite dynamics. Filters implemented by several missions were analyzed, including an Extended Kalman Filter in both the CSSWE mission (Gerhardt, 2014) and the MOVE-II mission (Messmann et al., 2017), and the Isotropic Kalman Filter in the UWE-2 mission (Schmidt et al., 2008). However, the complexity of implementing a Kalman Filter for a first CubeSat mission is high; a deep knowledge of state estimation must be attained and the development of the filter (both in the mathematical formulation as well as in the software implementation) is not trivial. Therefore, an alternative approach was selected.

There are several deterministic methods to determine attitude characteristics with a set of on-board measurements. Some of these methods focus on solv-



ing Wahba's Problem using two or more vector observations in two different coordinate systems to find the optimal rotation matrix between them (Vinther, 2011). In Markley and Mortari (1999), a series of attitude estimators were analyzed, and Vinther (2011) found the Singular Value Decomposition (SVD) method (proposed initially by Markley (1988)) to be more robust than other faster methods, such as the Fast Optimal Attitude Matrix (FOAM) or Estimator of the Optimal Quaternion (ESOQ) approaches.

Since attitude data was not required in real time to inform any of the satellite's functions, it could be analyzed on the ground ex post facto to provide an "image" of the satellite's orientation throughout orbits. Therefore, it was determined that measurements taken by the sensors described in the next subsection were to be processed on the ground via the SVD method to determine attitude, serving as baseline information that could inform the development of future attitude determination systems of our own, as well as others. Might there be any interest in the data collected on-orbit by the sensors on-board Quetzal-1's ADCS (or any other subsystem), you may contact the corresponding authors for this paper.

### 3.3. Sensors

An Adafruit breakout board for the Bosch BNO055 Inertial Measurement Unit (IMU), which contained a three-axis magnetometer, a three-axis gyroscope, and a three-axis accelerometer was selected for flight (Bosch, 2014). Such a selection was based on a trade study with variables of importance to this mission, such as: communication protocol, power consumption, operating voltage range, operating temperature, sensor range and resolution, as well as price. It was also important that the IMU was well documented and had a large community of users behind it. The accelerometer, however, was flown powered off as linear acceleration data while in free fall was deemed of little value on orbit. Additionally, 12 photodiodes (Vishay, Cat. No. TEMD6010FX01) were implemented as Sun sensors, two on each face of the satellite. Note that two were installed for redundancy in case of failure, as Gerhardt (2014) noted sensor degradation after one month of flight. The selected photodiodes had flight

heritage from CSSWE, and were digitized via a voltage divider and an Analog-to-Digital converter (Texas Instruments, Cat. No. ADC128D818). All sensors were sampled at a 0.1 Hz rate and controlled by an ATMEGA328P microcontroller implemented on the ADCS circuit board.

### 3.4. Magnetometer Calibration

A magnetometer typically suffers from four types of errors: hard iron errors, soft iron errors, scaling factors, and non-orthogonality errors. For simplicity and relevance, only hard and soft iron errors will be covered here. The first type is usually caused by either constant or time-varying magnetic fields that are present in the location of the magnetometer and offset the magnetic field being measured (i.e., Earth's magnetic field) (Springmann and Cutler, 2012). For Quetzal-1, a constant offset to the magnetometer measurement was expected to be caused by the permanent magnet located on the same PCB as the magnetometer.

Soft iron errors result from materials that generate a magnetic field in response to an external magnetizing field (Springmann and Cutler, 2012). Such a material on board the satellite was the pair of hysteresis rods, which generated a different field ( $\vec{B}$ ) for a given, magnetizing field ( $\vec{H}$ ). For this reason, the hysteresis rods were located as far away as possible from the magnetometer (see subsection 2.1.4).

The calibration method used for Quetzal-1 followed the steps and guidelines set by Springmann and Cutler (2012), where the proposed attitude-independent calibration technique performs a non-linear, least-squares fit to estimate the hard and soft iron calibration parameters. Being able to calibrate the magnetometer without knowledge of the satellite's attitude is important, as the calibrated measurements would then be used via the SVD method to attain attitude. The results of the calibration performed on a flight model of the ADCS PCB prior to launch are shown in Table 3 (subsection 4.3.2) alongside the results obtained via on-orbit calibration for ease of comparison.

## 4. On-Orbit Performance of Quetzal-1's ADCS

### 4.1. Detumbling and Stabilization

Table 3: Fitted Coefficients for On-ground (Prior to Launch) and On-orbit Magnetometer Calibration

Satellite Axes	Soft iron errors (scaling factors)			Hard iron errors (constant offsets)		
		On-ground calibration (ADCS PCB only)	On-orbit calibration		On-ground calibration (ADCS PCB only)	On-orbit calibration
X	$a$	1.0127	1.0218	$x_0$	0.5650	42.8907
Y	$b$	0.9897	0.9605	$y_0$	-5.4199	62.6603
Z	$c$	0.9478	1.2415	$z_0$	171.8728	163.6372

#### 4.1.1. First Weeks After Deployment

When the first data packets were received, 1 hour and 20 minutes after deployment, it was observed that the rotational rates for Quetzal-1 were oscillating between  $-25$   $^{\circ}/s$  and  $+25$   $^{\circ}/s$  in each axis. These were the rotational rates acquired upon deployment from the Kibo module aboard the ISS via the Japanese Experiment Module (JEM) Small Satellite Orbital Deployer (J-SSOD). Within a week (see Figure 5), these values decreased as expected, finally stabilizing the X axis between  $-3$   $^{\circ}/s$  and  $+1$   $^{\circ}/s$ , and the Y axis between  $-1$   $^{\circ}/s$  and  $+3$   $^{\circ}/s$ . The Z axis reached a minimum of  $+2.8$   $^{\circ}/s$  and stabilized to an operationally acceptable  $+3.5$   $^{\circ}/s$ ; since the magnet was placed in alignment to the satellite's Z axis, some rotation speed was expected to build up on this axis.

#### 4.1.2. Resulting steady-state error after detumbling

As mentioned in subsection 2.1.2, an angular offset  $\gamma$  between the permanent magnet's axis (aligned

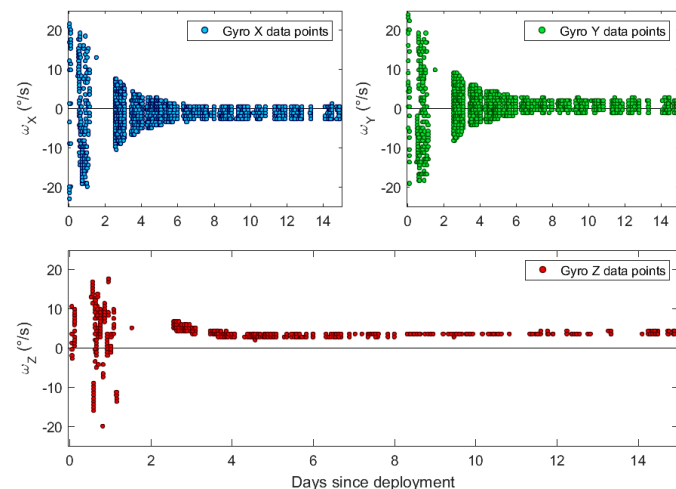


Figure 5. Quetzal-1's rotational rate over all axes during detumbling, as measured by gyroscope (weeks 1-2).

with the satellite's Z axis) and the magnetic field lines was expected (recall Figure 1). After deployment,  $\gamma$  was calculated using the magnetic vector measured by the on-board magnetometer. To note, the magnetic vector calculations were performed after the magnetometer was calibrated (further details in subsection 4.3.2). Typically, the offset between the magnetic vector ( $\vec{B}$ ) and the satellite's -Z axis remained between  $\gamma = 14.18^{\circ}$  and  $\gamma = 14.28^{\circ}$  (95% confidence interval). This offset caused the satellite's -Z axis to present a coning motion about the magnetic field lines. The presence of this motion was evidenced by the gyroscope measurements detailed in subsection 4.1.1, where Figure 5 shows that the rotational rates over the X and Y axes were not centered around 0  $^{\circ}/s$ .

#### 4.1.3. Satellite Stability Throughout the Mission

Following correct detumbling, data showed that, approximately one month after deployment, the rotational rate on the Z axis began to gradually increase. This increase was quite steep in the days prior to May 22, 2020 (as observed in the bottom plot shown in Figure 6), where the Z axis rotational rate increased from  $\sim 3$   $^{\circ}/s$  to  $\sim 8$   $^{\circ}/s$ .

#### 4.1.4. Effects of the Payload Filter Carousel on Satellite Stability

There were no active attitude control actuators on board the satellite intended to mitigate the rotational rate increase mentioned in the previous subsection. However, the actuation axis of the filter carousel (from the payload) was aligned to the Z axis, and this actuator did have an effect over the axis' rotation. The anodized aluminum carousel assembly, shown in Figure 7, had a total moment of inertia of 109.843 kg mm<sup>2</sup>.



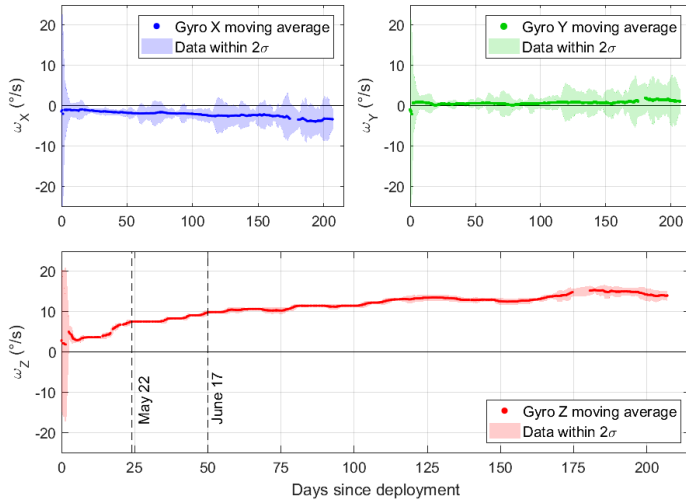


Figure 6: Quetzal-1's rotational rate over all axes through the life of the satellite as measured by three-axis gyroscope.

The TEKCELEO WLG-30 piezoelectric motor that actuated the carousel rotated at 126 rpm (Zea et al., 2023). Ground tests indicated that the carousel accelerated and decelerated at an equal rate when rotating, completing half a revolution in approximately 239 ms. This resulted in a maximum acceleration of  $55.18 \frac{\text{rad}}{\text{s}^2}$  and a  $6061.18 \mu\text{N} \cdot \text{m}$  torque over the satellite's Z axis.

Due to the symmetric nature of the acceleration and deceleration of the motor, the net torque over the Z axis was zero. However, an important detail was observed on orbit: As previously stated in subsection 4.1.2, the Z axis of the satellite was not parallel to the magnetic field lines on which the satellite rotated (as per PMAC behavior). This deviation of the satellite's axis of rotation  $\vec{\omega}_z$  with respect to its Z axis caused the carousel rotational speed to induce a gyroscopic torque over the X and Y axes, as evidenced by the following equations retrieved from (Steinmann, 2014):

$$\vec{K}_c = \vec{I}_c \cdot \vec{\omega}_c, \quad (3)$$

$$\vec{\tau}_{x,y} = \vec{K}_c \times \vec{\omega}_z, \quad (4)$$

where the carousel's angular momentum  $\vec{K}_c$  is the dot product of the carousel's moment of inertia  $\vec{I}_c$  and its angular velocity  $\vec{\omega}_c$  (126 rpm). The cross product of  $\vec{K}_c$  and the satellite's net rotational axis  $\vec{\omega}_z$  was non-zero due to the deviation between the vectors.

This resulted in a momentary torque over the satellite's XY-plane when the carousel rotated. Such a torque could cause a temporary increase in the oscillation amplitude of the satellite's X and Y axes. This was advantageous to the mission because the physical oscillations would increase the magnetizing field oscillations (also called H-field oscillations) on the hysteresis material; thus, increasing the conversion of kinetic energy into heat within the material (Gerhardt, 2014). These temporary misalignments may have acted as an angular momentum dumping method to counteract the rotational rate increase observed over the Z axis.

As a means of experimentation, and to prevent battery depletion due to the COMMS continuous transmission failures (further detailed in Aguilar et al. (2023), the on-board computer's watchdog reset timer cycle was decreased from 24 to six hours on May 22, and then further to two hours on June 17 (both instances marked by dashed lines in Figures 6 and 8). This caused the motor, which rotated on each reboot, to move by a revolution 12 times per day (instead of once per day) starting on June 17. Figure 6 previously showed the rotational rates throughout the whole mission, and Figure 8 details the changes in rotational acceleration.

Note that the acceleration shown in Figure 8 maintained (on average) positive values during the duration of the satellite's life. However, a decrease in magnitude was observed after the changes in periodicity of the filter carousel rotations (after May 22 and June 17). Figure 9 additionally shows that, although the rotational energy of the satellite increased throughout the mission, energy dips could still be detected (marked by letters A and B within the plot). Such is an indication that a rotational energy dumping mechanism was at play: either via the gyroscopic torque effect previously mentioned, the presence of altered external torques at those times, or a combination thereof. By the end of the mission on November 25 (211 days after deployment), the satellite reached a maximum rotational rate of  $+16.65 \text{ }^\circ/\text{s}$ . This rotational rate was still adequate to perform payload operations (Zea et al., 2022) and to guarantee adequate performance of the satellite's solar chargers (Aguilar-Nadalini et al.,

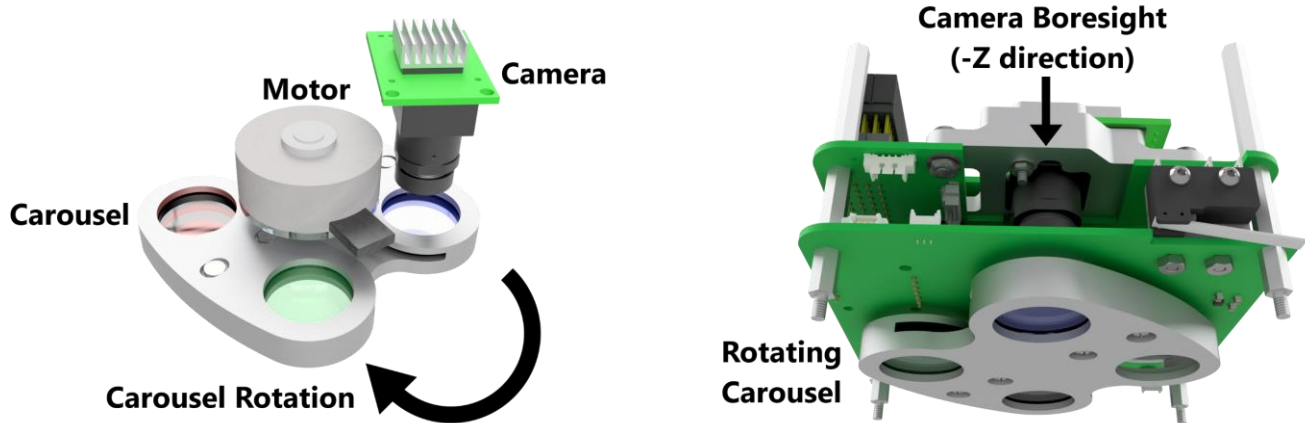


Figure 7. Quetzal-1 payload assembly, which included an aluminum carousel, a piezoelectric motor, and camera.

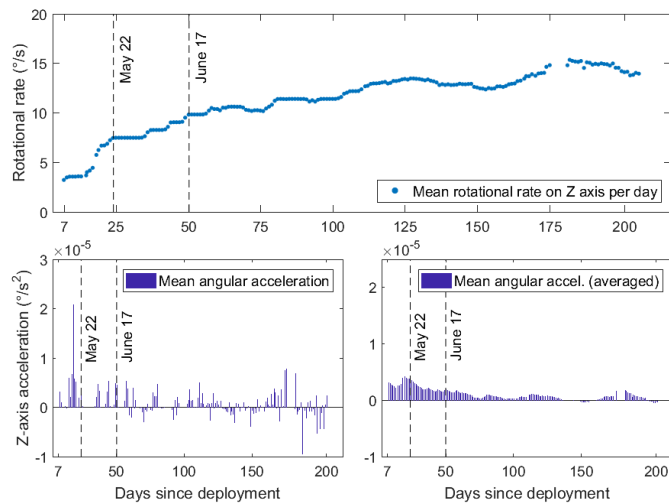


Figure 8: Mean rotational rate and acceleration over Quetzal-1's Z axis per day (Weeks 2-30). Lower two graphs show the 'raw' mean acceleration (left) and the averaged mean acceleration (right).

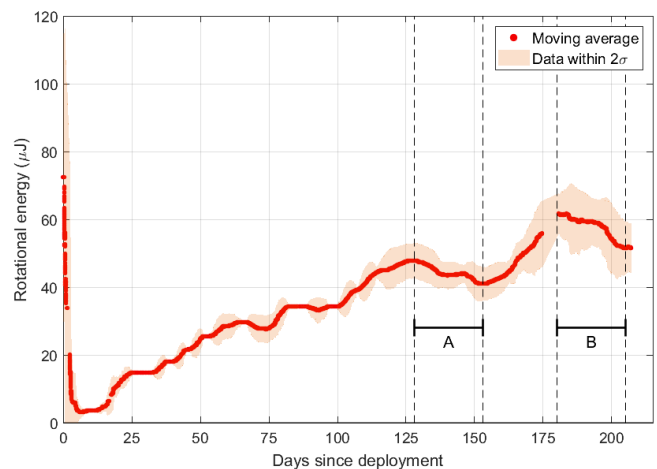


Figure 9: Net rotational energy of Quetzal-1 throughout the mission (long periods of energy decrease marked by letters A & B).

2023), but it is noteworthy for teams developing their own PMACs.

## 4.2. PMAC System Performance

The initial performance of the implemented PMAC system enabled stabilization in all axes within a week. The increase in rotational energy as the weeks progressed may have been caused by a combination of factors, including a possible underperformance of the available hysteresis material. Two factors come into play when attempting to explain this. First of all, the satellite did not align perfectly with the magnetic field (recall subsection 4.1.2). Such a misalignment caused the H-field applied to hysteresis rods to be off-center.

That is, the H-field oscillations are not symmetrical about 0 A/m (most prominently for the X axis rod, as seen in Figure 10). Secondly, the bar magnet (which was oversized with respect to the required minimum magnetic moment) also caused a constant offset of the H-field as seen by the hysteresis rods. As noted by Gerhardt (2014), an offset to the applied H-field results in a smaller and distorted hysteresis curve for a given rod, which reduces its damping capability. Therefore, both prior statements lead towards the supposition that the hysteresis rods were not operating at their maximum damping capacity. As a secondary note, possible magnetic sources within the satellite that may have caused the satellite's aforementioned misalignment could include current carrying traces

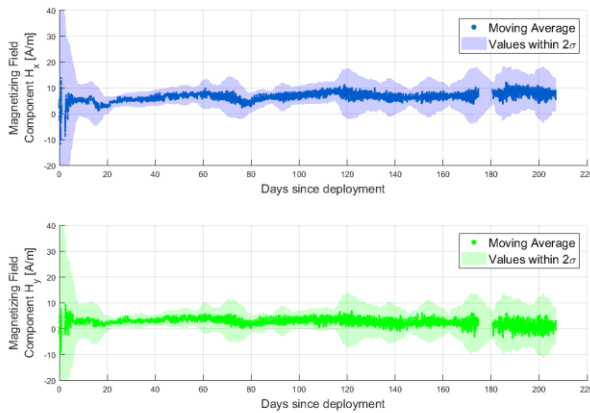
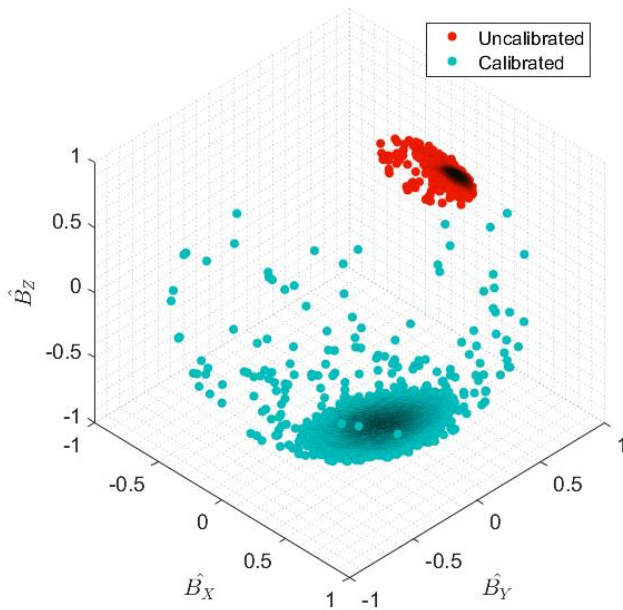


Figure 10. H-field oscillations experienced by satellite axes containing hysteresis rods (X and Y).



within the PCB, inductors present in the Electric Power System (EPS) PCB, the satellite's antennas or the voltage transformers present in the motor driver (Tekceleco, Cat. No. WLG 30).

### 4.3. Sensor Performance

#### 4.3.1. Gyroscope

The three-axis gyroscope performed nominally on orbit. Although no calibration was performed, the data

matched the expected behavior of the satellite, which presented a roll over the magnetic field lines. The gyroscope of the IMU did not present any glitch or failure throughout the mission despite the temperature variations between  $-14^{\circ}\text{C}$  and  $33^{\circ}\text{C}$  that the ADCS circuit board experienced. The board's temperature was measured by the thermal sensor integrated into the BNO055 IMU unit and by a secondary thermal sensor (Texas Instruments, Cat. No. TMP100-Q1). However, the gyroscope's measurement resolution of  $0.7844\text{ }^{\circ}/\text{s}$  proved to be inadequate because most rotational changes on orbit were smaller. Note that this coarse resolution was caused by the data being compressed into a single byte (as per on-board software design), as the gyroscope within the BNO055 IMU has a  $0.06\text{ }^{\circ}/\text{s}$  resolution within a  $\pm 2000\text{ }^{\circ}/\text{s}$  range (Bosch, 2014).

#### 4.3.2. Magnetometer

Table 3 shows the calculated calibration coefficients for Quetzal-1's magnetometer, as well as the results of the calibration performed prior to launch. Note that the  $z_0$  coefficient is largely similar in both scenarios because the bar magnet's magnetic field dominates the constant offset in this axis, while all other coefficients vary due to the presence of many other magnetic and electronic components in the fully-assembled satellite. Additionally, Figure 11 shows the direction of Earth's Magnetic Field vector  $\vec{B}$  with respect to the satellite's body frame. The red dots indicate the uncalibrated data measured by the magnetometer, influenced by the permanent magnet. The blue dots indicate the measured data after the magnetometer calibration was performed. The calibrated data shows vector  $\vec{B}$  typically oriented towards the  $-Z$  face of the satellite, as expected due to the PMAC system configuration.

Although magnetometer data was valuable, as it was fundamental in calculating the satellite's attitude throughout the mission using the methodology discussed in subsection 3.2, it was observed that the magnetometer of the IMU presented measurement glitches when operating at temperatures below  $10^{\circ}\text{C}$  combined with the vacuum of space. Below this threshold, the sensor occasionally transmitted all-zero magnetic data. The frequency of these incorrect measurements

increased when the board's temperature decreased, as shown in Figure 12.

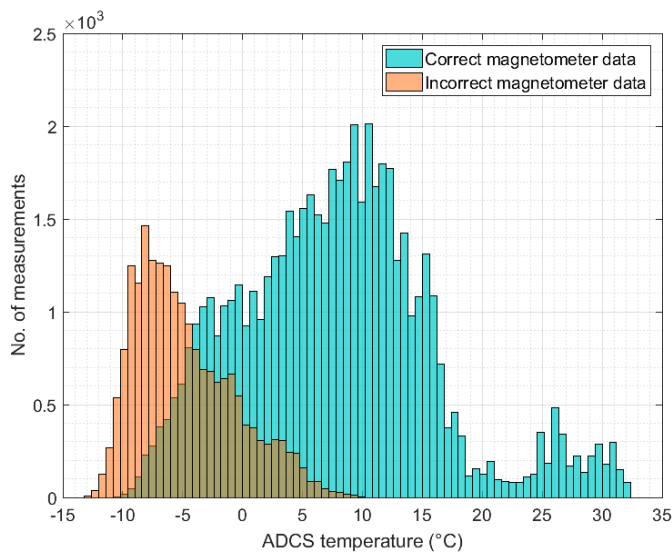


Figure 12. Incorrect magnetometer measurements distribution depending on temperature.

This behavior had been previously observed during thermal-vacuum ground tests (data not shown). However, the sensor was deemed fit for flight because thermal modeling showed the temperature of the board would remain mostly above 5°C when the satellite was in sunlight. The attitude determination algorithm required the measurements from the Sun sensors as well as from the magnetometer to estimate the satellite's attitude. For this reason, incorrect magnetometer measurements during eclipse periods did not severely compromise the module's operation. In Puglia et al. (2017), it is mentioned that the BNO055 IMU's gyroscopes failed under high vacuum conditions, but the magnetometer yielded reliable data. Note, however, that the sample rate used by Puglia et al. (2017) was 10 kHz, while Quetzal-1 sampled the IMU at a significantly lower rate of 0.1 Hz. Nonetheless, the results observed on orbit for Quetzal-1 are opposite, with the gyroscope transmitting reliable data and the magnetometer only partially operating.

#### 4.3.3. Coarse Sun Sensors

Using photodiodes on each satellite face, an estimate of the Sun's angle of incidence could be calculated by determining what percentage of its maximum

voltage a photodiode was outputting (via a voltage divider on the ADCS PCB). Prior to deployment, a constant maximum output voltage of 2.5 V was established for calculations on orbit. However, the maximum voltage of the photodiodes did not remain constant throughout the mission, but rather decreased in an exponential fashion, as shown in Figure 13. This phenomenon was most likely caused by the darkening of the plastic covers of the photodiodes due to UV radiation, as previously noted in Gerhardt (2014). Note that the maximum voltage curves for the +Z and -Z photodiodes shown in Figure 13 present peaks and troughs because there were periods during which these panels were hidden from the Sun, due to a combination of the orbit's orientation towards the Sun and the alignment of the satellite to Earth's magnetic field.

### 4.4. Attitude Determination

#### 4.4.1. Nadir Pointing Analysis

Due to the nature of the mission, it was important to estimate the angle between the camera's boresight (pointing towards the -Z face of the satellite) and nadir. This estimation was performed by using the SVD method to solve Wahba's problem, and the result was used to determine the orientation of the camera towards Earth's surface while the satellite was above Guatemala. The camera's field of view could then be approximated and compared to the pictures captured by the payload subsystem when commanded

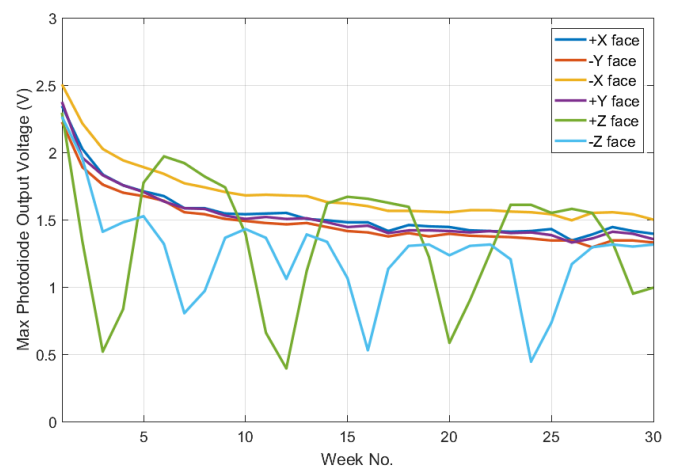


Figure 13. Photodiode maximum output voltage showing degradation on orbit.



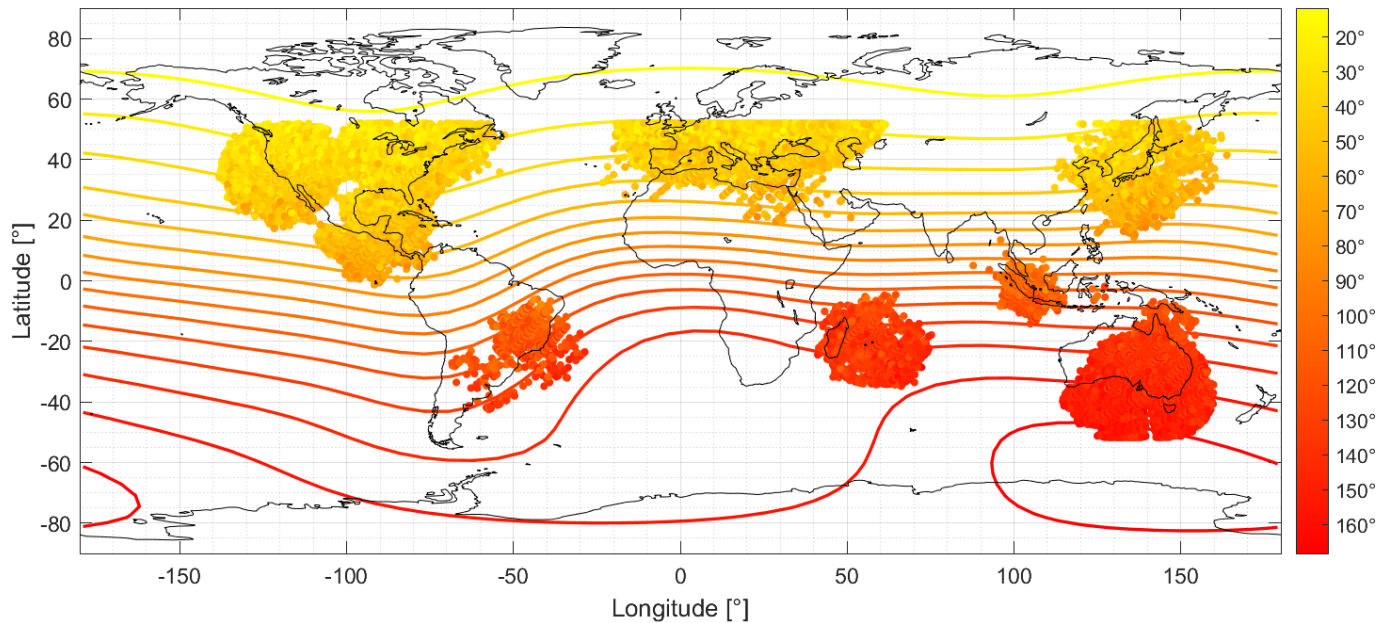


Figure 14. Angle between nadir and camera boresight (-Z) depending on location. Dots show experimental data, lines show theoretical data. Both lines and dots are color-coded in relation to the color bar on the right-hand side

by the ground control station in Guatemala. The method was written in MATLAB and the obtained results are shown in Figure 14. The plot shows curves indicating the theoretical angle between the camera boresight and nadir depending on the Earth's magnetic field inclination. It also shows superimposed dots corresponding to the locations of the satellite at times when a beacon was transmitted back to Earth. As observed, the results from the telemetry matched the theoretical calculations, indicating the adequate operation of the ADCS module.

Figure 15 shows the distribution of angles between nadir and -Z depending on latitude. As expected, the angle increased in the southern hemisphere due to the magnetic field inclination below the Equator. The camera boresight was approximately parallel to the Earth's surface when the satellite was near the equator, and the angle continued to decrease when the satellite moved towards the geographical north. The red curve shows the moving average of the angle calculated with a window of 5° in latitude. The pink shade shows the interval encompassing 95% of the data, and the black dots show individual data points. The angle dispersion

on every latitude was the result of the satellite's coning motion (recall subsection 4.1.2).

To further analyze the satellite's camera orientation when the satellite passed over Guatemala, the histogram shown in Figure 16 was plotted. The normal distribution of angles had a mean angle of  $\mu = 48.06^\circ$

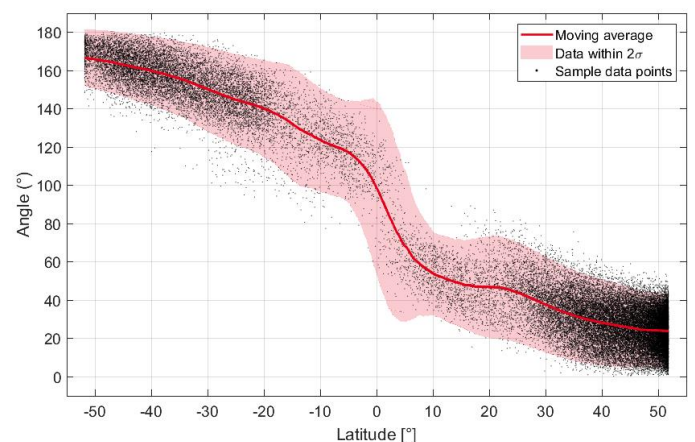


Figure 15. Angle between nadir and camera boresight (-Z) depending on latitude (only data captured along the continent of America was taken into account, so as to discard natural variations in Earth's magnetic field that occur as longitude increases towards the east).

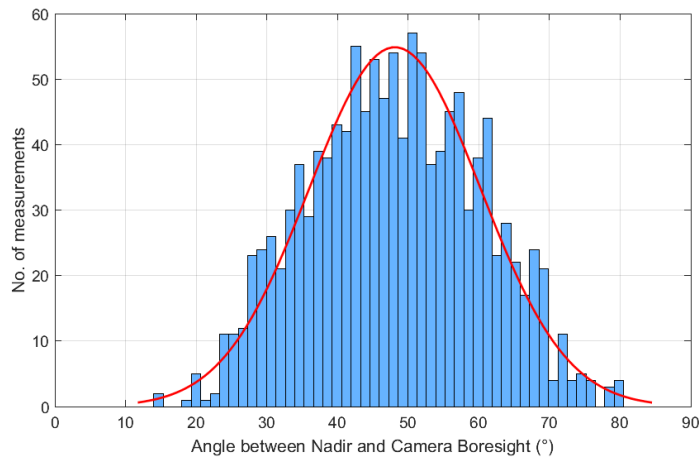
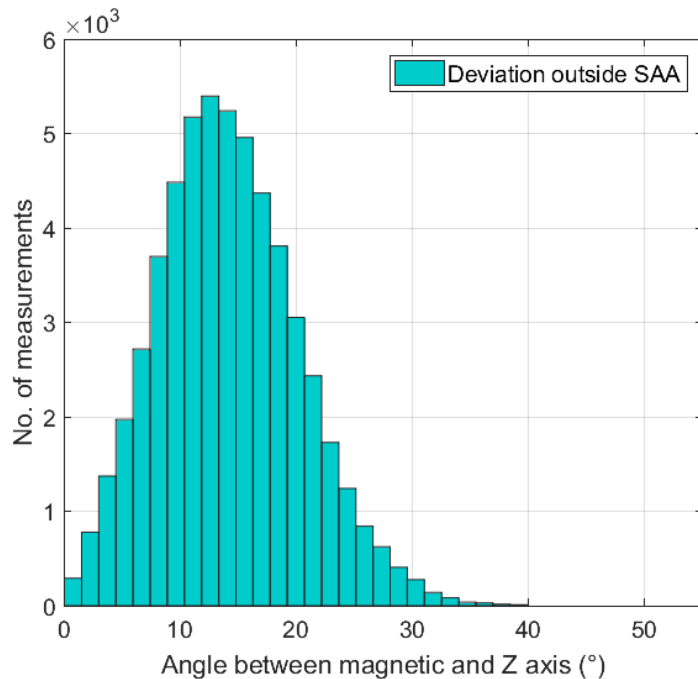


Figure 16: Angle distribution between nadir and Camera boresight (-Z) during Guatemala overflights.

$\pm 0.88^\circ$  (99% CI). This result was similar to the theoretical  $\sim 45^\circ$  magnetic field inclination indicated by the IGRF-12 magnetic field model over Guatemala (see Figure 2). It evidenced accurate pre-flight modeling and adequate satellite orientation for payload operations. The standard deviation of the aforementioned angle distribution was  $\sigma = 12.14^\circ$ . This dispersion was in line with the estimated coning angle,  $\gamma$ , of the camera boresight's axis (-Z axis) about the magnetic field vector (see subsection 4.1.2).



#### 4.5. Effects of the South Atlantic Anomaly (SAA)

The SAA is a weak spot in Earth's magnetic field near the coast of Brazil where the magnetic intensity drops below 32,000 nT. This dent in the magnetic field occupies a region between the  $-50^\circ$  and  $0^\circ$  latitudes, and between the  $-90^\circ$  and  $+40^\circ$  longitudes. It represents a risk to the electrical circuits on board satellites, as well as in the ISS, due to high energy particles that dip closer to the Earth's surface (Prölss, 2004). Besides the radiation effects, the SAA can also have a direct effect on passive orientation systems that rely on the magnetic field's intensity. The control authority of the permanent magnet on board Quetzal-1 diminished when the satellite crossed the SAA because of the low field intensity that ranged from 21,500 nT to 30,000 nT, as measured by the on-board magnetometer. It caused the magnet's torque to drop to approximately half, compared to the nominal torque outside the SAA, according to Eqn.1. This resulted in an increase in oscillation amplitude on the X and Y axes of the satellite, which in turn increased the misalignment of the satellite's Z axis with respect to the magnetic field lines. Figure 17 shows the distribution of offset angles ( $\gamma$ )

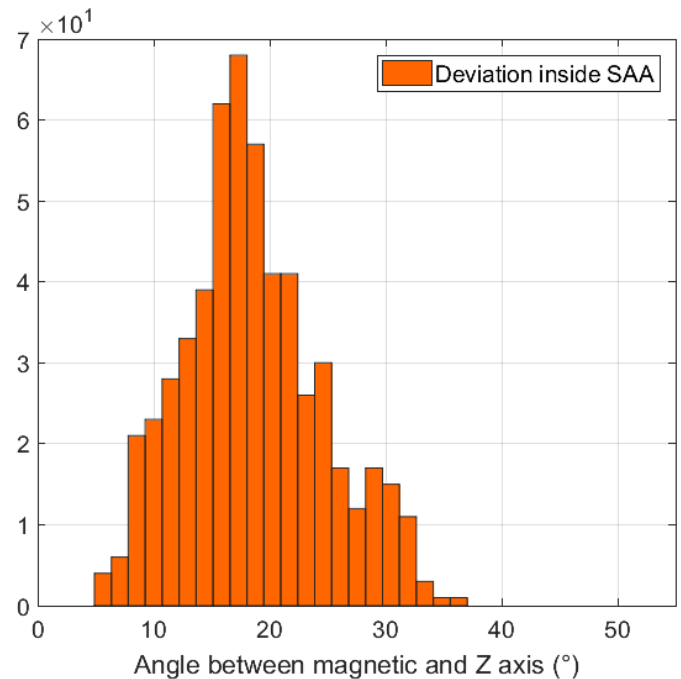


Figure 17: Distribution of offset angles between Z axis and magnetic field vector (outside and inside SAA).



between the Z axis of the satellite and the magnetic field vector outside the SAA, as well as inside of it.

The distribution of offset angles outside the SAA had a mean of  $\gamma_1 = 14.19^\circ \pm 0.05^\circ$  (95% CI) and  $\sigma_1 = 6.03^\circ$ , while the distribution of angles inside the SAA had a mean of  $\gamma_2 = 18.55^\circ \pm 0.50^\circ$  (95% CI) and  $\sigma_2 = 6.05^\circ$ . Therefore, it shows an increased pointing error when Quetzal-1 was traveling through the magnetic field's weak spot.

## 5. Conclusions

A permanent magnet with a magnetic moment of  $\|\vec{m}_{magnet}\| = 0.7363 \text{ A} \cdot \text{m}^2 \geq \|\vec{m}_{min}\|$  was selected. The magnet's north pole faced the -Z direction, thus aligning the satellite's camera boresight towards nadir over the northern hemisphere. This design decision enabled the camera to take relevant imagery over Guatemala. Upon deployment, the satellite acquired initial rotational rates between  $-25^\circ/\text{s}$  and  $+25^\circ/\text{s}$  on each axis. These values decreased as expected within a week, finally stabilizing the X axis between  $-3^\circ/\text{s}$  and  $+1^\circ/\text{s}$ , and the Y axis between  $-1^\circ/\text{s}$  and  $+3^\circ/\text{s}$ . The Z axis reached a minimum of  $+2.8^\circ/\text{s}$ , and stabilized to an operational-acceptable  $+3.5^\circ/\text{s}$ . Following detumbling, a gradual increase in rotational speed accumulated on the satellite's Z axis. By the end of the mission on November 25th (211 days after deployment), the satellite reached a maximum rotational rate on the Z axis of  $+16.65^\circ/\text{s}$ . More details regarding the end of the mission can be found in (Aguilar-Nadalini et al., 2023). This rotational rate was still adequate to perform payload operations and to guarantee adequate performance of the satellite's solar chargers.

The satellite's Z axis did not perfectly align with the magnetic field, rather the angle between said axis and the magnetic field vector remained between  $\gamma = 14.18^\circ$  and  $\gamma = 14.28^\circ$  (95% confidence interval). This is explained by the existence of other magnetic components within the satellite. Such a misalignment provided gyroscopic torque on each carousel rotation, which may have provided a rotational energy dumping mechanism via the hysteresis rods; however, said misalignment also caused the H-field applied to the hysteresis rods to be off-center. In such a case, the hysteresis rods' damping capability is reduced. Further reduc-

tion of this damping capability is caused by the constant H-field offset applied by the bar magnet. These two items, in conjunction, lead to the supposition that the hysteresis material was not operating at its maximum damping capacity (thus permitting the accumulation of rotational energy on the Z axis).

The magnetometer behaved nominally at temperatures above  $10^\circ\text{C}$ , but transmitted all-zero data with an increasing frequency as the temperature reached its minimum of  $-14^\circ\text{C}$ . The photodiodes were critical in determining the solar vector position, but suffered from UV degradation as time progressed. Initial voltage measured through a voltage divider on the ADCS circuit board was 2.5 V, but 211 days after deployment the voltage decreased to approximately 1.5 V.

The angle between the satellite's camera boresight and nadir over Guatemala had a normal distribution with mean  $\mu = 48.06^\circ \pm 0.88^\circ$  (99% CI) and standard deviation  $\sigma = 12.14^\circ$ . This matched the expected magnetic inclination over Guatemala as predicted by the IGRF-12 model. Finally, the SAA had a direct effect on the PMAC system. The control authority of the permanent magnet on board Quetzal-1 decreased when the satellite crossed the SAA, as evidenced by an increase in oscillation amplitude on the X and Y axes of the satellite that was observed while within this area.

## 6. Recommendations

Regarding photodiode degradation, note that two sets of equal photodiodes were placed on each satellite side for redundancy, and both sets suffered approximately equal degradation. It would have been beneficial to include asymmetrical redundancy; namely, placing photodiodes from different manufacturers.

Although the selected IMU had been tested in vacuum on Earth, it did not possess clearly documented flight heritage. Selecting an IMU, or separate gyroscope and magnetometer sensors for that matter, that had flight heritage might have led to fewer issues, especially focusing on the glitches the on board magnetometer suffered at low temperatures. For further missions, we can recommend the use of the gyroscope on board this module. However, we cannot recommend the use of the magnetometer on board the IMU, due to

the temperature-induced glitches that were observed on orbit.

To missions that might already be integrating a rotating carousel for an Earth-facing sensor, it may prove beneficial to set the PMAC system in such a way that the least-controlled axis is left collinear to the axis of rotation of said carousel. As with Quetzal-1, this might provide gyroscopic torque that could reduce rotational energy through the hysteresis rods, provided there is a misalignment between the satellite's rotational axis and the carousel's rotation axis.

## Acknowledgments

The authors thank Universidad del Valle de Guatemala for its support, which made this project possible. CubeSat safety reviews, and launch and deployment from the International Space Station were provided under KiboCUBE, a joint program of the United Nations Office for Outer Space Affairs (UNOOSA) and Japan Aerospace Exploration Agency (JAXA). Environmental testing was done thanks to the support of the United Kingdom Space Agency (UKSA) and ASTROSAT. The authors would like to acknowledge and thank Dr. David Gerhardt, Dr. Julio Gallegos and M.Sc. Pablo Oliva for the invaluable support provided to the development of this subsystem. Dr. Gerhardt is also acknowledged for reviewing this manuscript. We would also like to thank Mr. Kendy Cipriano for his immaculate work soldering the electronic components on Quetzal-1's circuit boards, and Mrs. Estela Morales for supporting the project's administrative activities. Finally, a large debt of gratitude is owed to all those students, professors, advisors and organizations who made this project and especially this subsystem, possible.

## References

Aguilar-Nadalini, A. et al. (2023): Design and On-Orbit Performance of the Electrical Power System for the Quetzal-1 CubeSat, *J. of Small Satellites (JoSS)*, Vol. 12, No. 2, p. 1201–1229. Available at: [www.jossonline.com](http://www.jossonline.com).

- Alvarez, D. (2019): CubeSat Phase: 5, Module: Attitude Determination and Control System, Undergraduate Thesis, Universidad del Valle de Guatemala, Guatemala City. [Unpublished thesis.]
- Birnie, J. et al. (2023): Novel Approach for Structural Finite Element Analysis on CubeSat's Bolted Connections. [Unpublished manuscript.]
- Bosch (2014): Intelligent 9-Axis Absolute Orientation Sensor. Available at: [https://cdn-shop.adafruit.com/datasheets/BST\\_BNO055\\_DS000\\_12.pdf](https://cdn-shop.adafruit.com/datasheets/BST_BNO055_DS000_12.pdf) (accessed Oct. 18, 2021).
- Chung, K. et al. (2023): Design, Development, and Pre-Flight Testing of the Fault-Tolerant Command and Data Handling Subsystem of the Quetzal-1 Nanosatellite. [Unpublished manuscript.]
- Danchik, R. J. (1998): An Overview of Transit Development, *Johns Hopkins Apl Technical Digest*, Vol. 19(1), p. 9. Available at: <https://www.xnatmap.org/adnm/pub/timeserv/danchik.pdf> (accessed Oct. 18, 2021).
- Gerhardt, D. (2014): Small Satellite Passive Magnetic Attitude Control. Available at: <https://scholar.colorado.edu/concern/graduate-thesis-or-dissertations/s1784k881> (accessed Oct. 18, 2021).
- Markley, F. L. (1988): Attitude Determination Using Vector Observations and the Singular Value Decomposition, *J. of the Astronautical Sciences*, Vol. 36(3), pp. 245–258. Available at: [http://www.malcolmdshuster.com/FC\\_Markley\\_1988\\_J\\_SVD\\_JAS\\_MDSscan.pdf](http://www.malcolmdshuster.com/FC_Markley_1988_J_SVD_JAS_MDSscan.pdf) (accessed Oct. 18, 2021).
- Markley, F. L. and Mortari, D. (1999): How to Estimate Attitude from Vector Observations, *Astrodynamics Specialist*. Available at: <https://ntrs.nasa.gov/citations/19990104598> (accessed Oct. 18, 2021).
- Martínez, M. et al. (2018): Guatemala's Remote Sensing CubeSat - Tools and Approaches to Increase the Probability of Mission Success, in *32nd Ann. AIAA/USU Conf. on Small Satellites*, Logan, UT. Available at: <https://digitalcommons.usu.edu/cgi/viewcontent.cgi?article=4288&context=smallsat> (accessed Oct. 18, 2021).
- Messmann, D., Grübler, T., Coelho, F. et al. (2017): Advances in the Development of the Attitude Determination and Control System of the CubeSat

- MOVE-II. Available at: <https://www.eucass.eu/doi/EUCASS2017-660.pdf> (accessed Oct. 18, 2021).
- National Geophysical Data Center (n.d.): NCEI Geomagnetic Calculators. U. S. Depart. Commerce. Available at: <https://www.ngdc.noaa.gov/geomag/calculators/magcalc.shtml#igrfgrid> (accessed Jan. 30, 2021).
- Princeton Satellite Systems (2010): Cubesat Control Toolbox. Available at: <https://www.psatsatellite.com/products/sct/cubesat-toolbox/> (accessed Oct. 18, 2021).
- Prölss, G. (2004): *Physics of the Earth's Space Environment: An Introduction*, Berlin Heidelberg: Springer-Verlag. doi: 10.1007/978-3-642-97123-5.
- Pugia, S. et al. (2017): Quad-Thruster FEMTA Micropropulsion System for CubeSat 1-Axis Control. Available at: <https://digitalcommons.usu.edu/cgi/viewcontent.cgi?filename=0&article=3544&context=smallsat&type=additional> (accessed Oct. 20, 2021).
- Santoni, F. and Zelli, M. (2009): Passive Magnetic Attitude Stabilization of the UNISAT-4 Microsatellite, *Acta Astronautica*, Vol. 65(5), pp. 792–803. doi: 10.1016/j.actaastro.2009.03.012.
- Schmidt, M., Ravandoor, K., Kurz, O. et al. (2008): Attitude Determination for the Pico-Satellite UWE-2, *IFAC Proc. Volumes*, Vol. 41(2), pp. 14,036–14,041. doi: 10.3182/20080706-5-KR-1001.02376.
- Springmann, J. C. and Cutler, J. W. (2012): Attitude-Independent Magnetometer Calibration with Time-Varying Bias, *J. of Guidance, Control, and Dynamics*, Vol. 35(4), pp. 1080–1088. doi: 10.2514/1.56726.
- Steinmann, P. (2014): How Gyros Create Stabilizing Torque. Available at: [http://veemmarine.com/wp-content/uploads/2015/11/White\\_Paper\\_1403-How\\_Gyros\\_Create\\_Stabilizing-Torque.pdf](http://veemmarine.com/wp-content/uploads/2015/11/White_Paper_1403-How_Gyros_Create_Stabilizing-Torque.pdf) (accessed Oct. 18, 2021).
- Taniguchi, F., Akagi, H., and Matsumoto, K. (2020): KiboCUBE - UNOOSA/JAXA Cooperation Program for Capacity Building by Using the Innovative CubeSat Launch Opportunity from ISS Kibo, *Space Capacity Building in the XXI Century*, Vol. 22, pp. 85–94. doi: 10.1007/978-3-030-21938-3-8.
- Vinther, K. (2011): Inexpensive CubeSat Attitude Estimation Using Quaternions and Unscented Kalman Filtering, *Automatic Control in Aerospace*, Vol. 4. Available at: [https://vbn.aau.dk/ws/portalfiles/portal/71439993/Inexpensive\\_CubeSat\\_Attitude\\_Estimation\\_Using\\_Quaternions\\_and\\_Unscented\\_Kalman\\_Filtering.pdf](https://vbn.aau.dk/ws/portalfiles/portal/71439993/Inexpensive_CubeSat_Attitude_Estimation_Using_Quaternions_and_Unscented_Kalman_Filtering.pdf) (accessed Oct. 18, 2021).
- Zea, L. et al. (2016): A Methodology for CubeSat Mission Selection, *J. of Small Satellites (JoSS)*, Vol. 5(3), pp. 483–511. Available at: <https://jossonline.com/wp-content/uploads/2021/08/Final-Zea-A-Methodology-for-CubeSat-Mission-Selection.pdf> (accessed Oct. 18, 2021).
- Zea, L. et al. (2023): Multispectral Imaging Payload for 1U CubeSats - Design and Development Considerations, and Spaceflight Operations and Results. [Unpublished manuscript.]